

X-ray photodesorption and proton destruction in protoplanetary disks: pyrimidine

Edgar Mendoza^{1*}, G. C. Almeida², D.P.P. Andrade³, H. Luna⁴, W. Wolff⁴,
M. L. M. Rocco² & H. M. Boechat-Roberty¹

¹Observatório do Valongo, Universidade Federal do Rio de Janeiro - UFRJ, Ladeira Pedro Antônio 43, CEP 20080-090, Rio de Janeiro, RJ, Brazil

²Instituto de Química, Universidade Federal do Rio de Janeiro - UFRJ, Ilha do Fundão, CEP 21949-900, Rio de Janeiro, RJ, Brazil

³Instituto de Pesquisa e Desenvolvimento, Universidade do Vale do Paraíba, Av. Shishima Hifumi, 2911, CEP 12244-000 São José dos Campos, SP, Brazil

⁴Instituto de Física, Universidade Federal do Rio de Janeiro - UFRJ, Ilha do Fundão, CEP 21949-900, Rio de Janeiro, RJ, Brazil.

Received / Accepted

ABSTRACT

The organic compounds HCN and C₂H₂, present in protoplanetary disks, may react to form precursor molecules of the nucleobases, such as the pyrimidine molecule, C₄H₄N₂. Depending on the temperature in a given region of the disk, molecules are in the gas phase or condensed onto grain surfaces. The action of X-ray photons and MeV protons, emitted by the young central star, may lead to several physical and chemical processes in such prestellar environments.

In this work we have experimentally investigated the ionization, dissociation and desorption processes of pyrimidine in the condensed and the gas phase stimulated by soft X-rays and protons, respectively. Pyrimidine was frozen at temperatures below 130 K and irradiated with X-rays at energies from 394 to 427 eV. In the gas phase experiment, a pyrimidine effusive jet at room temperature was bombarded with protons of 2.5 MeV. In both experiments, the time-of-flight mass-spectrometry technique was employed. Partial photodesorption ion yields as a function of the X-ray photon energy for ions such as C₃H₂⁺, HC₃NH⁺ and C₄H⁺ were determined.

The experimental results were applied to conditions of the protoplanetary disk of TW Hydra star. Assuming three density profiles of molecular hydrogen, 1×10^6 , 1×10^7 and 1×10^8 cm⁻³, we determined HC₃NH⁺ ion-production rates of the order of 10^{-31} up to 10^{-8} ions cm⁻³ s⁻¹. Integrating over 1×10^6 yr, HC₃NH⁺ column density values, ranging from 3.47×10^9 to 1.29×10^{13} cm⁻², were obtained as a function of the distance from central star. The optical depth is the main variable that affects ions production. In addition, computational simulations were used to determine the kinetic energies of ions desorbed from pyrimidine ice distributed between ~ 7 and 15 eV.

Key words: Astrochemistry – methods: laboratory – Protoplanetary Disks: X-ray – Organic molecules – ice – ionization

1 INTRODUCTION

Several organic molecules have been identified in different objects of the interstellar medium (ISM) such as: HCN, CH₃CN (Solomon et al. 1971), CH₃C₃N (Brotten et al. 1984), HC₁₁N (Bell et al. 1997) and C₃H₇CN (Belloche et al. 2009). Ionized and neutral species have been detected in several protoplanetary disks, including CO, CO₂, CN, HCN, HNC, H₂CO, C₂H, C₂H₂, CS, OH, HCO⁺, H¹³CO⁺, DCO⁺, N₂H⁺ and water vapour (Dutrey, Guilloteau &

Guelin 1997; Kastner et al. 1997; Qi et al. 2003; Thi, van Zadelhoff & van Dishoeck 2004; Carr & Najita 2008, Pontoppidan et al. 2010). The molecular pathways responsible for the formation of more complex molecules are not well established. However, it is known that polymerization reactions of HCN (hydrogen cyanide) and C₂H₂ (acetylene) lead to the formation of aromatic compounds containing Nitrogen atoms such as the pyrimidine molecule (1,3-Diazine) (Mitchell, Huntress & Prasad 1979; Frenklach & Feigelson 1989; Ricca, Bauschlicher & Bakes 2001; Cernicharo 2004). Pyrimidine (C₄H₄N₂) consists of a benzenic ring with two N atoms substituting two C-H groups at the positions 1 and 3, and is a component of the DNA and RNA nucleobases uracil, thymine and cy-

* E-mail: emendoza@astro.ufrj.br

tosine, shown in Figure 1. Pyrimidine can also lead to the formation of compounds called polycyclic aromatic nitrogen heterocycle molecules (PANHs). Observational surveys have been devoted to the search for pyrimidine. Kuan et al. 2003 analyzed sub millimeter emission lines of pyrimidine in three massive star-forming regions: Sgr B2(N), Orion KL and W52 e1/e2, which upper limits of the order of 10^{14} cm $^{-2}$ were determined. Charnley et al. 2005 performed surveys towards IRC+10216, a carbon-rich AGB star, searching for the basic units of PANHs, such as pyridine (C $_5$ H $_5$ N), pyrimidine (C $_4$ H $_4$ N $_2$) and the two aromatic rings species quinoline and isoquinoline (C $_9$ H $_7$ N). They obtained the upper limits ($\sim 10^{13}$ cm $^{-2}$) for all species, except for pyrimidine.

The possible precursor molecules of pyrimidine were detected in the protoplanetary nebula CRL 618: C $_6$ H $_6$, HCN, HC $_3$ N, HC $_5$ N and HC $_7$ N (Cernicharo et al. 2001, Thorwirth et al. 2003, Pardo, Cernicharo & Goicoechea 2005), where column density values of $\sim 5 \times 10^{15}$, 2×10^{18} , 2.5×10^{17} , 8.3×10^{16} and 1.4×10^{16} cm $^{-2}$ were determined, respectively. In the experimental work of Hudgins et al. 2005, an unidentified line at 6.2 μ m, present in the spectral emission of planetary nebulae (PNe) and asymptotic giant branch (AGB), could be associated to molecules such as PANHs of ≥ 30 C atoms, according to the position of the N atom in the carbon skeleton structure.

Peeters et al. 2005 compared the UV photostability of benzenic ring, with 1, 2 and 3 N atoms, with that of C $_6$ H $_6$ (benzene). They found that the half-lives of these species in the diffuse interstellar medium (ISM) decrease, from years to days, with the increase of the number of N atoms in the ring. In addition, PANHs in the ISM can condense on the surface of grains, whose principal component is H $_2$ O (~ 90 %). In this way, Elsila et al. 2006 observed that mixtures of quinoline with H $_2$ O frozen at a temperature of 20 K when exposed to UV radiation lead to the substitution of oxygen atom in the rings of quinoline. This may elucidate the oxidation susceptibility that PANHs suffer in astrophysical ice analogs. Nuevo, Milam & Sandford 2012 have found that mixtures of NH $_3$:pyrimidine and H $_2$ O:NH $_3$:pyrimidine when exposed to UV radiation lead to the formation of prebiotic molecules such as uracil, cytosine and glycine. These results could explain the formation of nucleobases in the Solar Nebula. With respect to the formation of small PANHs, Ricca, Bauschlicher & Bakes 2001 present a study about reactions that produce nitrogenated aromatic molecules in conditions of Titan's atmosphere, their results show that the addition of HCN or C $_2$ H $_2$ in an aromatic ring implies an activation barrier of ~ 0.65 eV molecule $^{-1}$. This required energy can be provided by the solar UV-flux or by charged particles coming from the magnetosphere of Saturn.

The genesis of planetary systems takes place in protoplanetary disks, mainly in the planet-forming zone (≤ 50 AU) where a copious chemistry occurs (Bergin 2009). The young central stars have strong magnetic fields, and due to the intense magnetic reconnection events, they are strong emitters of X-ray photons and MeV protons that propagate into the circumstellar matter (Feigelson & Montmerle 1999). X-ray luminosities ranging from $L_X = 10^{28.5}$ to $10^{31.5}$ ergs s $^{-1}$, which corresponds to 10^4 times the solar luminosity (Glassgold, Najita, Igea 1997), also contribute to the disk material accretion onto the stellar surface which generates a huge amount of energetic photons (Gorti, Dullemond & Hollenbach 2009).

As X-ray photoabsorption cross-sections are significantly lower than the cross-section for UV photons, X-ray can penetrate greater distances within the disk, except in extremely dense regions ($n \gg 1 \times 10^8$ cm $^{-3}$), as at the mid-plane of the disk (Owen et

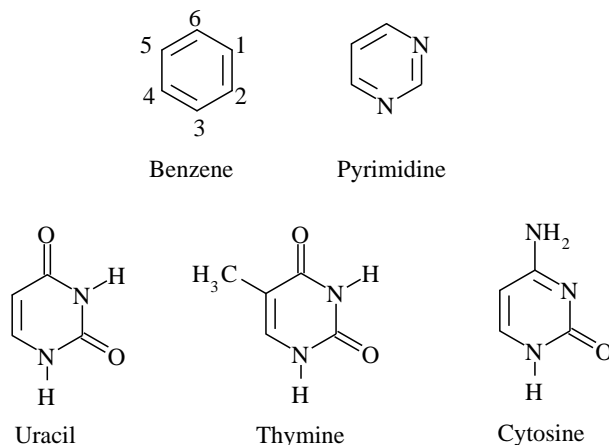


Figure 1. Molecular structure of benzene, pyrimidine and pyrimidinic nucleobases uracil, thymine and cytosine. The pyrimidine is a benzenic ring with two N atoms substituting two C-H groups at the positions 1 and 3.

al. 2009; Bethell & Bergin 2011). The so-called snow line in protoplanetary disks is a cold region distant from a central star where simple molecules condense onto grain surfaces forming icy mantles. UV and X-ray photons, electron and ion interactions may induce several chemical reactions in the ice, contributing to the formation, destruction and desorption of neutral and ionized species from the ice. In order to investigate these processes, several experimental simulations on the interaction of different agents with interstellar ice analogs have been performed (Bennett & Kaiser 2007; Andrade et al. 2010; Shanker et al. 2011; Pilling et al. 2012).

In the present experimental work, we study X-rays interaction with frozen pyrimidine, analyzing the photodesorbed ions from ice, and the destruction of pyrimidine in the gas phase caused by protons. The paper is organized as follows. In section 2 we described the experimental setup and the procedures to obtain the experimental results. In section 3 we discuss the relevant chemical reactions and pathways of the fragmentation of pyrimidine and present the mass spectra, the ion yields and the kinetic energies of the fragment ions extracted from these spectra. In section 4 the experimental data are applied to determine the values of relevance to the astrochemistry, as the ions production rates, the column densities and the half-life of pyrimidine ice in conditions of the protoplanetary disk of the TW Hydra star. Finally in the last section, we present a summary of the astrochemical experimental values and main conclusion of this work.

2 EXPERIMENTAL METHODS

2.1 X-ray photodesorption from pyrimidine ice

X-ray irradiation of pure pyrimidine ice was carried out at the Brazilian synchrotron light source (LNLS), employing photons with energies around N 1s $\rightarrow \pi^*$ resonance (399 eV), selected by the Spherical-Grating Monochromator (SGM). The electron storage ring operation mode was the single-bunch, when the photon-beam is pulsed in a period of 310.88 ns, with pulse width of ~ 60 ps and a rate of ~ 1550 photons bunch $^{-1}$ (Marques, Onisto & Tavares 2003). Figure 2 shows a schematic view of the experimental setup

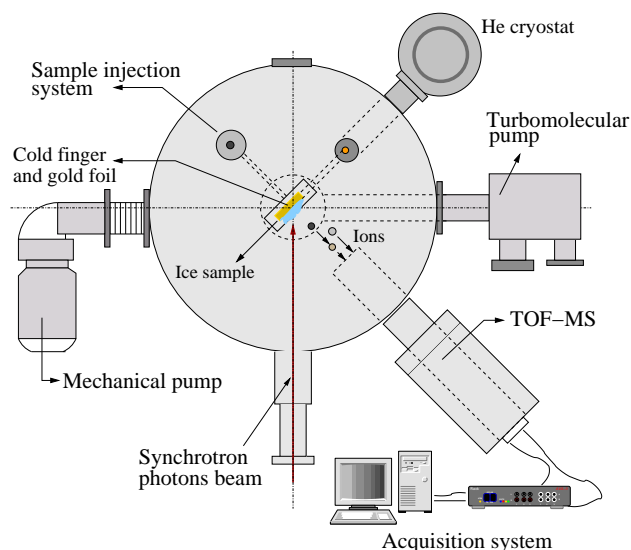


Figure 2. Experimental setup for measurements of X-ray photodesorption from condensed molecules, using the time of flight mass spectrometry (TOF-MS).

that consists in a cryostat, a sample injection system and a time-of-flight mass spectrometer housed in an ultra-high vacuum chamber maintained at a pressure of about 10^{-9} Torr. During the experiments the helium cryostat was held at a temperature of 130 K. At room temperature the sample of pyrimidine, commercialized by Sigma-Aldrich[®] with 99 % purity, is liquid but its vapor pressure is sufficient to produce a high gas density. The gas sample was introduced in the system by a thin tube placed nearby the sample holder, while the pressure near the holder was maintained at 1×10^{-6} Torr during 5 minutes. Pyrimidine was deposited on a thin gold foil of $1 \text{ cm} \times 1 \text{ cm}$ area and thickness of 0.001 mm, being the sample size larger than the photon beam spot of $\approx 0.075 \times 0.37 \text{ mm}$ (Farias, Jahnel & Lin 1997). The target thickness under such injection conditions is on the order of μm . The pulsed photon-beam interacts with the frozen sample placed at 45° with respect to the incident beam. The desorbed ions are mass and charge analyzed by the time-of-flight mass spectrometer, TOF - MS. This spectrometer consists basically of an electrostatic ion extraction system, a drift tube and a pair of microchannel plates (MCP), disposed in the Chevron configuration. After extraction, positive ions travel through three metallic grids (each with a nominal transmission of $\sim 90\%$), before reaching the MCP. The output signal of the fragment ions detector was processed by a standard pulse counting system, and provides the stop signal to the time-to-digital converter (TDC). The spectrometer potential was chosen such that ions with up to 10 eV initial kinetic energy and initial angular spread of up to 90° were directed to the ion detector. The synchrotron radiation (SR) timing pulse of 476.066 MHz, delivered by the microwave cavity of the storage ring, was processed by a 1/148 divider. This signal was used to trigger the experiment, as the start signal of the TDC. In order to select precisely the energies around the N 1s resonance, Near Edge X-Ray Absorption Fine Structure (NEXAFS) spectra were acquired.

2.2 Ion trajectory simulations

In order to obtain the TOF values, ion trajectory simulations employing the SIMION[®] software were done. The program was

compiled to a matrix of single-charged ions with masses ranging from 1 to 100 atomic mass unit, varying the initial kinetic energy (k_i) from 0 to 16 eV for each ion. The simulated TOF (t_s) was determined by using the standard expression:

$$t_s = \frac{d}{\sqrt{2V}} \sqrt{\frac{m}{q}}, \quad (1)$$

where d is the length of the flight tube, m/q is the mass-charge ratio and V is the applied extraction voltage.

In the single-bunch mode, all spectra are taken in the time-window of $\sim 310.88 \text{ ns}$. However, the TOF of each ion may be much longer than 310.88 ns. Consequently, the position of each ion within this time-window will be determined by the ratio TOF/310.88. The integer part of this quotient corresponds to the number of the SR photon cycles, and the fractional component defines the position within the time-window.

2.3 Proton collision with pyrimidine in the gas phase

The proton collision with the pyrimidine molecule was carried out at the Laboratory of Atomic and Molecular Collisions (LA-CAM) at the Universidade Federal do Rio de Janeiro.

In the experiment H^+ of 2.5 MeV, produced from a Source of Negative Ions (H^-) by Cesium Sputtering (SNICS II) and stripped to H^+ at the terminal voltage cell of the tandem accelerator (Pelletron[®] of 1.7 MV), were directed to the collision chamber. The proton beam interacts perpendicularly with the pyrimidine molecules effusing from a gas jet needle of 1 mm diameter after being cleaned and positioned by a pair of parallel plate electrostatic analyzers. Pyrimidine molecules were delivered through a clean vacuum line degassed by means of several freeze-pump-thaw cycles. The typical operating chamber pressure was of 1×10^{-6} torr, whereas the ultra-high vacuum beam line was kept at a base pressure of 3×10^{-8} torr. The ionic fragments and the ejected electrons were extracted from the interaction region by a two-field-time-of-flight mass spectrometer by applying a uniform electric field perpendicular to both the ion beam and molecular gas-jet.

While the dissociation products were detected by a MCP detector, the ejected electrons were directed in the opposite direction of the ions and detected by a channel electron multiplier (CEM). The detector signals from the MCP and CEM were recorded after proper amplification and discrimination from noise using standard nuclear electronics for fast pulses.

The ejected electron (start signal) was measured in coincidence with the ionic fragment (stop signal) produced by the ionizing event. The TOF spectra were acquired in multi-hit mode by a 250 ps time bin, 4 GHz multiple-event time digitizer interfaced to a computer. Several fragment ions were recorded in coincidence to obtain information on correlated dissociation products (Wolff et al. 2012). The resolving power of the detection system, the ratio between the higher and lower full width at half maximum values (FWHM), corresponding to the 38 (HCCCH^+) and 30 (N_2H_2^+) m/q respectively, was $\Delta t_{38}/\Delta t_{31} \sim 10$. The mass analysis of the spectra was made through a calibration using Kr gas. The fragmentation-yields uncertainties are between 10 and 20 %.

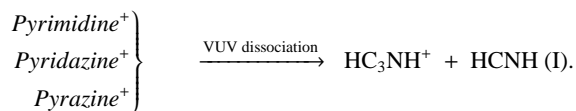
3 RESULTS AND DISCUSSION

3.1 Dissociation of pyrimidine due to X-rays and protons

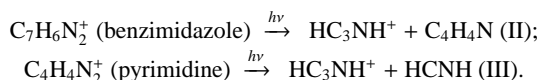
Figure 3a shows the spectra of the ions desorbed from pyrimidine ice at 130 K, due to X-rays interactions at three different en-

ergies, 394, 399 and 401 eV. The ions were detected in the time-window of 310.88 ns and, as mentioned in section 2.2, the identification of the fragment ion species was performed through the determination of the TOF for each ion. Structures depicted in Figure 3a show peak contributions of different ionic fragments. The overlapping peaks were deconvoluted in order to obtain the area of each fragment and from them the partial ion yields were determined. In Figure 3b, the partial ion yields of all observed fragments as a function of mass to charge ratio, m/q , are presented. The partial yields were defined as the ratio between each fragment peak and the sum of all areas, and thereby it was possible to quantify the photofragmentation channels of the pyrimidine ion ($C_4H_4N_2^+$) due to X-ray irradiation. In Table 1 these results are summarized.

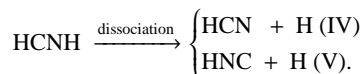
The most abundant fragment corresponds to the ion of $m/q = 52$ that was attributed to the HC_3NH^+ (protonated cyanoacetylene) ion, without ruling out the possible contribution of $NCCN^+$ and $C_4H_4^+$. Fondren et al. 2007 studied the pyrimidine (298 K) dissociation by different single charged heavy ions at low impact energies between 14 and 21.56 eV, identifying in all cases the HC_3NH^+ with abundances $> 3\%$. Similarly, but bombarding with photons at energies of 13.8, 15.7 and 23 eV, Vall-llosera et al. 2008 detected all impact energies the HC_3NH^+ ion with intensities $\geq 25\%$. In their work, the production of the HC_3NH^+ ion from dissociation of the isomers pyridazine and pyrazine ($C_4H_4N_2$) was also investigated. These isomers differ from the pyrimidine only by the position of the N atoms on the ring.



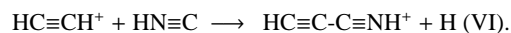
Here the chemical equations are numbered using Roman numerals. Schwell et al. 2008 studied the dissociative photoionization of N-heterocycles induced by synchrotron radiation at energies from 7 to 18 eV, using the mass spectrometry technique. The HC_3NH^+ ion was produced via the following dissociation channels



These experimental results were complemented with thermochemical data in order to give support that the HC_3NH^+ ion was the more probably fragment of $m/q = 52$. Tachikawa, Iyama & Fukuzumi 2003 calculations argued that the neutral fragment HCNH could explain the $[HCN]/[HNC]$ branching ratio in the interstellar medium, through the following reactions



Showing that the reaction IV preferentially occurs in the threshold energy region. The HC_3NH^+ ion was detected for the first time toward TMC-1 with a column density about $1 \times 10^{12} \text{ cm}^{-2}$ (Kawaguchi et al. 1994), and since the 1980s its formation mechanisms have been studied. Knight et al. 1986 proposed a mechanism that involves the cyclic $C_3H_3^+$ ion, one of the most stable organic molecules, and a N atom. However, the presence of a π -electron pair on the plane of $C_3H_3^+$ prevents the reaction of N atom substitution. For this purpose, Takagi et al. 1999 proposed, by means of quantum computations, an alternative route given by:



This reaction is the most probable one in comparison with the reaction $HC\equiv CH^+ + HC\equiv N$, since in this case it is necessary that the

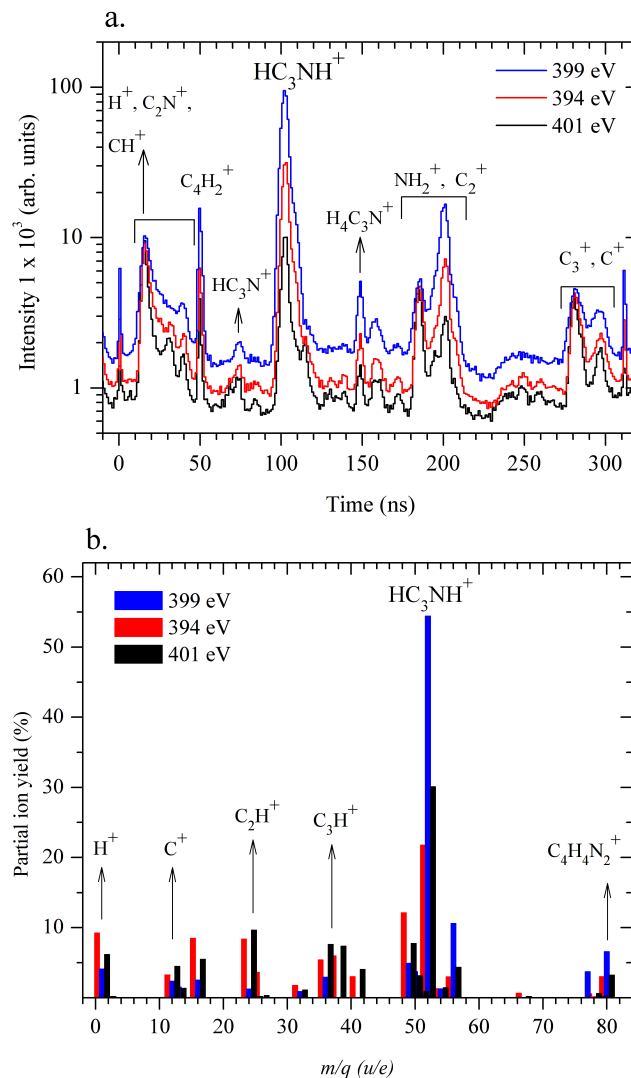
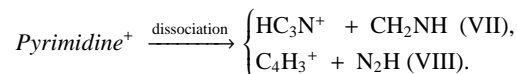


Figure 3. a. Ions desorbed from pyrimidine ice due to X-rays interaction at energies of 394 (red), 399 (blue) and 401 eV (black) and detected in the time-window of 310.88 ns; b. partial ion yield of fragments desorbed from icy pyrimidine.

hydrogen migrates via tunneling effect. On the other hand, it was identified the HC_3N^+ ion (cyanoacetylene, $m/q = 51$) with abundance of 0.9 % and the dissociation channels are:



However, due to the high ion yield of HC_3NH^+ , we believe that the dissociation channel (VII) is the more probable. Lin et al. 2006 have performed experiments on VUV-ionization of gaseous pyrimidine and they determined that photons at energy of 11.6 eV is capable of generating ionized cyanoacetylene, whose ionization energy is ~ 11.4 eV. In interstellar conditions, the electron recombination reaction $HCCCNH^+ + e^-$ produces HCCCN, HCCNC and maybe HNCCC isomers. It is known that the abundance ratios between these isomers in TMC-1 is $[HCCCN]:[HCCNC]:[HNCCC] = 1000:8:1$ (Kawaguchi et al. 1992), so that the reaction should be regioselective. Based on these observations, Fukuzawa & Osamura

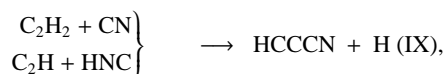
Table 1. Photodissociation pathways of pyrimidine ice stimulated by X-rays photons at 394 eV.

C ₄ H ₄ N ₂ + hν		394eV	C ₄ H ₄ N ₂ ⁺ + e ⁻ (6.35 %)
Ion	dissociation		Ionic fragment ^a + Neutral fragment ^b
C ₄ H ₄ N ₂ ⁺	21.7%		(HC ₃ NH ⁺ or C ₂ N ₂ ⁺) + (HCNH or C ₂ H ₄)
	12.1%		C ₄ H ⁺ + N ₂ H ₃
	9%		H ⁺ + C ₄ H ₃ N ₂
	8.4%		(NH ₂ ⁺ or CH ₄ ⁺) + (C ₄ H ₂ N or C ₃ N ₂)
	8.4%		C ₂ ⁺ + C ₂ H ₄ N ₂
	5.9%		(C ₂ N ⁺ or C ₃ H ₂ ⁺) + (C ₂ H ₄ N or CH ₂ N ₂)
	5.4%		C ₃ ⁺ + CH ₄ N ₂
	3.6%		(C ₂ H ₂ ⁺ or CN ⁺) + (C ₂ H ₂ N ₂ or C ₃ H ₄ N)
	3.2%		C ⁺ + C ₃ H ₄ N ₂
	3.0%		(HCN ₂ ⁺ or H ₃ C ₂ N ⁺) + (C ₃ H ₃ + C ₂ HN)
	2.9%		C ₂ H ₄ N ₂ ⁺ + C ₂
	2.7%		(C ₄ H ₂ ⁺ or C ₃ N ⁺) + (N ₂ H ₂ or CH ₄ N)
	1.8%		N ₂ H ₄ ⁺ + C ₄
	1.5%		CH ⁺ + C ₃ H ₃ N ₂
	1.3%		H ₄ C ₃ N ⁺ + CN
0.9%		(HC ₃ N ⁺ or C ₄ H ₃ ⁺) + (H ₃ CN or N ₂ H)	
0.6%		C ₃ H ₃ N ₂ ⁺ + CH	
0.6%		H ₂ ⁺ + C ₄ H ₂ N ₂	
0.5%		H ₃ C ₃ N ⁺ + HCN	
0.15%		C ₄ H ₃ N ₂ ⁺ + H	

^aMolecular ions with the same m/q ratio;

^bNeutral remnant with the same molecular mass.

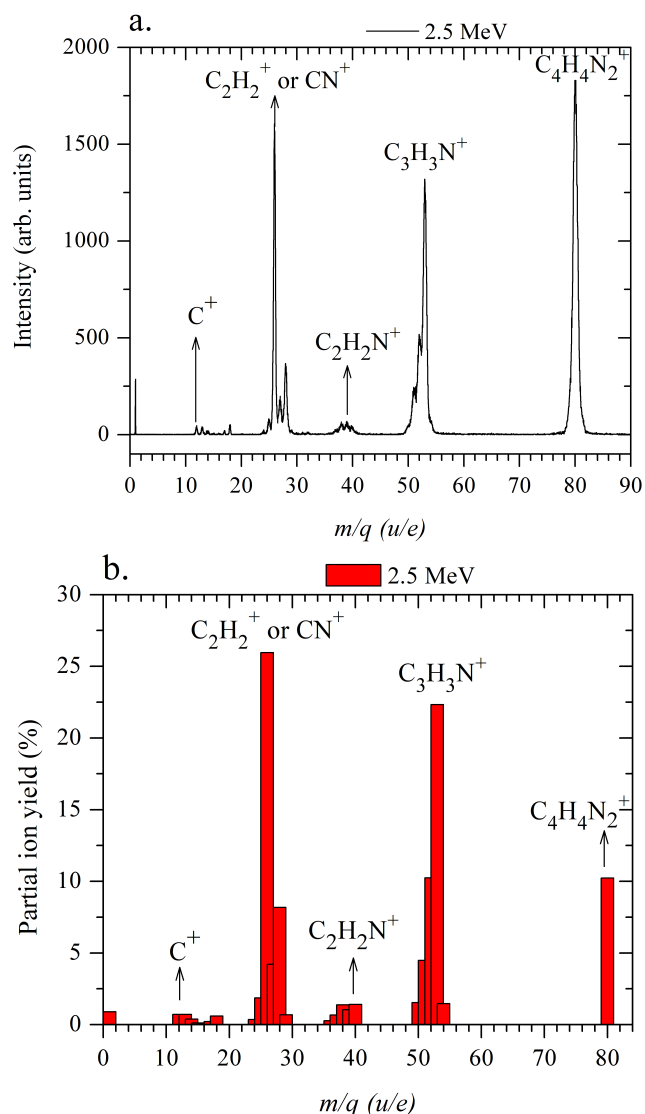
1997 proposed the following mechanisms



which are exothermic reactions and have no energy barrier, constituting the dominant neutral-neutral mechanism producer of HC-CCN.

A small peak at ~ 125 ns, that corresponds to the $m/q = 53$ fragment, has a partial ion yield of about 0.5 %. Experimental and theoretical studies indicate that the HCN ($m/q = 27$) is a typical fragment from N-heterocycle dissociations. If we consider the HCN the likely neutral fragment from pyrimidine ice, the $m/q = 53$ ion must be C₃H₃N⁺ (vinyl cyanide). The second option would be the channel that generates N≡C-C≡N⁺-H (protonated cyanogen) + C₂H₃. Notwithstanding, it is expected that at lower temperatures the protonation of cyanogen molecule should be an inefficient reaction (Petrie, Millar & Markwick 2003). The vinyl cyanide ion has not yet been confirmed in the ISM, however its formation mechanisms are being studied. Bera, Lee & Schaefer 2009 have proposed a mechanism via C₂H₂⁺ + HCN reaction, which leads to the formation of the HCC(H)NCH neutral isomer.

The C≡C-C≡C-H⁺ ion (butadiynyl) was identified with a branching ratio of 12.1 %. The neutral equivalent was detected for the first time in IRC+10216 (Guelin, Green & Thaddeus 1978), whose column densities are between 4×10^{14} and 3×10^{15} cm⁻². Theoretical studies indicate that the molecule is linear, Senet & Hochlaf 2010 found that the bond lengths are C₁:C₂ = 1.2164 Å, C₂:C₃ = 1.3765 Å, C₃:C₄ = 1.2118 Å and C₄:H = 1.0635 Å. For the


Figure 4. a. Time of flight mass spectrum of gas phase pyrimidine dissociated by protons at energy of 2.5 MeV ; b. Partial ion yield as a function of the mass charge ratio, m/q .

cyclic isomer (less stable) the bond lengths proposed would be C₁:C₂ = C₂:C₃ = 1.4555 Å, C₁:C₄ = C₃:C₄ = 1.3998 Å and C₄:H ($< 180^\circ$) = 1.0707 Å. A curious fact is that the negative ion C₄H⁻ was also observed in the carbon star IRC+10216, being up to date the second of the six anions detected in the ISM with a ratio of [C₄H]/[C₄H⁻] = 4200 (Cernicharo et al. 2007).

The H-C≡C-H⁺ ($m/q = 26$) and the C₄H₂⁺ ($m/q = 50$) were measured with a yield $\lesssim 4$ %. For the latter, there are two structures: (i) where both hydrogens are at the end of the carbon skeleton, forming a cumulene (H₂C=C=C=C⁺), (ii) the hydrogen atoms are at both ends of the carbon chain, forming the butadiyne ion (H-C≡C-C≡C-H⁺). Both molecules have already been detected at interstellar conditions, $N(\text{H}_2\text{C}_4) \sim 7.5 \times 10^{12}$ cm⁻² in TMC 1 (Kawaguchi et al. 1991) and $N(\text{HC}_4\text{H}) \sim 1.2 \times 10^{17}$ cm⁻² in CRL 618 (Cernicharo et al. 2001). However, Kawaguchi et al. 1991 demonstrated that the butadiyne is energetically (~ 1.9 eV) more stable than H₂CCCC, so that the more likely structure for $m/q = 50$ would be H-C≡C-C≡C-H⁺. Among other ions of astrochemistry

Table 2. Dissociation pathways of the gas phase pyrimidine by protons at 2.5 MeV.

Ion	dissociation	Fragmentation
$C_4H_4N_2 + H^+$	$\xrightarrow{2.5MeV}$	$C_4H_4N_2^+ + e^-$ (10.2 %)
$C_4H_4N_2^+$	$\xrightarrow{25.9\%}$	$(C_2H_2^+ \text{ or } CN^+) + (C_2H_2N_2 \text{ or } C_3H_4N)$
	$\xrightarrow{22.3\%}$	$H_3C_3N^+ + HCN$
	$\xrightarrow{10.2\%}$	$(HC_3NH^+ \text{ or } C_2N_2^+) + (HCNH \text{ or } C_2H_4)$
	$\xrightarrow{8.2\%}$	$(H_2CN^+ \text{ or } C_2H_4^+) + (HC_3NH \text{ or } C_2N_2)$
	$\xrightarrow{4.5\%}$	$(HC_3N^+ \text{ or } C_4H_3^+) + (H_3CN \text{ or } N_2H)$
	$\xrightarrow{4.2\%}$	$(HCN^+ \text{ or } C_2H_3^+) + (H_3C_3N + HC_2N_2)$
	$\xrightarrow{1.86\%}$	$C_2H^+ + C_2H_3N_2$
	$\xrightarrow{1.53\%}$	$(C_4H_2^+ \text{ or } C_3N^+) + (N_2H_2 \text{ or } CH_4N)$
	$\xrightarrow{1.5\%}$	$H_4C_3N^+ + CN$
	$\xrightarrow{1.4\%}$	$(C_2H_2N^+ \text{ or } NCN^+) + (C_2H_2N + C_3H_4)$
	$\xrightarrow{1\%}$	$(HC_2N^+ \text{ or } C_3H_3^+) + (H_3C_2N + HCN_2)$
	$\xrightarrow{0.897\%}$	$H^+ + C_4H_3N_2$
	$\xrightarrow{0.70\%}$	$C^+ + C_3H_4N_2$
	$\xrightarrow{0.70\%}$	$CH^+ + C_3H_3N_2$
	$\xrightarrow{0.69\%}$	$H_3CN^+ + HC_3N$
	$\xrightarrow{0.67\%}$	$C_3H^+ + H_3CN_2$
	$\xrightarrow{0.38\%}$	$(N^+ \text{ or } CH_2^+) + (C_4H_4N \text{ or } C_3H_2N_2)$
	$\xrightarrow{0.36\%}$	$C_2^+ + C_2H_4N_2$
	$\xrightarrow{0.27\%}$	$C_3^+ + CH_4N_2$

^aMolecular ions with the same m/q ratio;^bNeutral remnant with the same molecular mass.

interest, we detected the C^+ , C_2^+ and C_3^+ ions, with partial yields of 3.2 %, 8.4 % and 5.4 %, respectively.

In Figure 4b and Table 2 are presented the mass spectrum due to proton interaction at 2.5 MeV with gas phase pyrimidine and dissociation pathways, respectively. Our results point out that X-ray photons produce more fragmentation than protons. Using X-ray photons, the HC_3NH^+ and C_4H^+ ions contribute ~ 34 % of the ion production, while the $\sim 66\%$ remainder is distributed among eighteen ions (≤ 9 %). Using protons, the ion yields of the $C_2H_2^+$, $H_3C_3N^+$, HC_3NH^+ and $C_4H_4N_2^+$ ions are ~ 68 %, the ~ 32 % remainder being due to the contribution of sixteen ions. This behavior is due to (i) the photon energy-range of the X-rays is around the $N\ 1s \rightarrow \pi^*$ resonance, (ii) the condensed phase provides a scenario which favors electronic rearrangements, so that a greater number of fragment ions are formed before being photodesorbed.

For ions with m/q from 12 to 14, corresponding to C^+ , CH^+ , CH_2^+ (or N^+), ion yields of ~ 0.7 , 0.7 and 0.38 % respectively, were determined. On the other hand, ion series with m/q from 24 to 29, corresponding to C_2^+ , HCC^+ , CN^+ , HCN^+ , H_2CN^+ and H_3CN^+ were detected. Worth noting that the last three ions have high yields, being the CN^+ the most intense (~ 25.9 %), although the $C_2H_2^+$ also contributes to such percentage. A curious fact is that comparing the H_2CN^+ and H_3CN^+ ions, the H_3CN^+ has a higher yield, which leads us to consider a migration mechanism of two H atoms during the transition state of the reaction *pyrimidine*⁺ + H.

Ions with m/q between 36 to 40 were detected with yields of ≤ 1.4 %, among which the most intense ion was the $m/q = 40$ that can have contributions of $C_2H_2N^+$ and NCN^+ fragments. The family of HC_3N^+ , HC_3NH^+ and $H_2C_3NH^+$ ions was also iden-

tified. However, the yield of HC_3NH^+ was ~ 10 %, while for X-rays it was ~ 22 %.

In both experiments, we observe that the pyrimidine is widely fragmented by photons and protons. However, this molecule survives more to proton impact than X-ray interaction, since the channels $C_4H_4N_2 + h\nu \rightarrow C_4H_4N_2^+$ and $C_4H_4N_2 + H^+ \rightarrow C_4H_4N_2^+$ were ~ 6 and 10 %, respectively.

3.2 Photodesorption ion yield

In order to quantify the production of ions by the X-ray photodesorption process from pyrimidine ice, the photodesorption ion yield (Y_i) for each ion i was determined by means of

$$Y_i = \frac{A_i}{n_{ph} N_b}, \quad (2)$$

where A_i is the deconvoluted peak area of the ion i , n_{ph} the number of photons per bunch (see § 2.1), that depends on the electron current injection into the acceleration ring, and N_b is the number of bunches, which reaches values about 1×10^9 bunches per measurement. In Table 3, we present the Y_i values determined for several ions at photon energies of 394, 398, 399, 400, 401, 408 and 427 eV. The desorption ion yields were determined with uncertainties < 21.7 %.

In Figure 5, it is shown the behavior of the Y_i for some ions as a function of the photon energy in the range from 394 to 427 eV. The major Y_i values are those obtained at 399 eV, the N1s resonance energy, where the photoabsorption cross section is higher. However, this tendency is more pronounced for HC_3NH^+ (10^{-7} ion photon⁻¹), among others. This means that the photodissociation pathways in pyrimidine ice preferentially occur between 1, 2 and 3, 4 bonds (see Figure 1). On the other hand, when $E \gtrsim 400$ eV, the Y_i for all detected ions drop-off. The H^+ , C^+ , $C_2H_2^+$ and $C_3H_2^+$ yields are the most affected by the highest energy here used, since their Y_i fall from 10^{-8} to 10^{-10} ion photon⁻¹.

3.3 Kinetic energies of ions desorbed from ice

Ions of same mass m to charge q ratio may photodesorb from the icy surface with different kinetic energies, K_{pd} , arriving at the detector with different times of flight t , causing peak broadening Δt . In our experiments, all the desorbed ions are accelerated by the same extraction voltage V (4500 V). Therefore, the standard expression applies

$$\frac{t}{2\Delta t} = \frac{K_{pd} + qV}{\Delta K_{pd}}, \quad (3)$$

The contribution of the kinetic energy of a given ion is obtained by the FWHM ($2\Delta t$) of its peak (Guilhaus 1995). Considering that $qV \gg K_{pd}$, equation 3 reduces to

$$\frac{t}{2\Delta t} \approx \frac{qV}{\Delta K_{pd}}, \quad (4)$$

being qV constant, $t/2\Delta t$ hardly depends on K_{pd} . On the other hand, the distribution of photodesorption velocities (v_{pd} , cm s⁻¹) can be estimated by means of

$$v_{pd} = v - E \left(\frac{q}{m} \right) t, \quad (5)$$

where E is the electric field, t is the TOF and v the velocity in the drift tube. Simulating the trajectories of ions of same mass to charge ratio, varying K_{pd} between 0 and 16 eV with a step of 2 eV,

Table 3. Photodesorption ion yield from pyrimidine ice by X-rays at energies from 394 to 430 eV.

m/q	Ionic Fragment	Photodesorption yield (ions/photon)						
		394 eV	398 eV	399 eV	400 eV	401 eV	408 eV	427 eV
1	H ⁺	$1.4(2) \times 10^{-8}$	$1.6(6) \times 10^{-8}$	$3(1) \times 10^{-8}$	$1.2(6) \times 10^{-8}$	$7(2) \times 10^{-9}$	$4(1) \times 10^{-9}$	$2(1) \times 10^{-10}$
2	H ₂ ⁺	$9(3) \times 10^{-10}$	$1.6(6) \times 10^{-8}$	$8(3) \times 10^{-10}$	$7(4) \times 10^{-10}$	$2(1) \times 10^{-10}$	-	-
12	C ⁺	$4.9(4) \times 10^{-9}$	$9.7(8) \times 10^{-9}$	$1.61(7) \times 10^{-8}$	$7.5(7) \times 10^{-9}$	$5.4(8) \times 10^{-9}$	$3.1(8) \times 10^{-9}$	$9(3) \times 10^{-10}$
13	CH ⁺	$2.3(4) \times 10^{-9}$	$2.4(9) \times 10^{-10}$	$1.0(5) \times 10^{-9}$	$3.4(9) \times 10^{-9}$	$1.6(5) \times 10^{-9}$	$8(2) \times 10^{-10}$	-
16	NH ₂ ⁺ or CH ₄ ⁺	$1.30(4) \times 10^{-8}$	$1.53(1) \times 10^{-8}$	$1.7(3) \times 10^{-8}$	$9(1) \times 10^{-9}$	$6.5(3) \times 10^{-9}$	$2.6(3) \times 10^{-9}$	-
24	C ₂ ⁺	$1.3(1) \times 10^{-8}$	$7(3) \times 10^{-9}$	$9(3) \times 10^{-9}$	$6(2) \times 10^{-9}$	$1.1(1) \times 10^{-8}$	$7(2) \times 10^{-9}$	-
26	C ₂ H ₂ ⁺ or CN ⁺	$6(4) \times 10^{-9}$	$5(1) \times 10^{-10}$	-	$4(1) \times 10^{-9}$	$4(2) \times 10^{-10}$	$8(3) \times 10^{-10}$	-
36	C ₃ ⁺	$8(3) \times 10^{-9}$	$9(6) \times 10^{-9}$	$2.04(6) \times 10^{-8}$	$6(3) \times 10^{-9}$	$9.1(5) \times 10^{-9}$	$3.7(4) \times 10^{-9}$	$1.4(3) \times 10^{-9}$
38	C ₂ N ⁺ or C ₃ H ₂ ⁺	$9.2(8) \times 10^{-9}$	$2.16(9) \times 10^{-8}$	-	$1.2(5) \times 10^{-9}$	$9(3) \times 10^{-9}$	$2.8(6) \times 10^{-9}$	$4(2) \times 10^{-10}$
41	HCN ₂ ⁺ or H ₃ C ₂ N ⁺	$4.6(7) \times 10^{-9}$	$8(5) \times 10^{-9}$	-	-	$5(2) \times 10^{-9}$	$2.0(8) \times 10^{-9}$	$8(3) \times 10^{-10}$
49	C ₄ H ⁺	$1.8(1) \times 10^{-8}$	$1.8(4) \times 10^{-8}$	$3.4(3) \times 10^{-8}$	$1.1(4) \times 10^{-8}$	$9(2) \times 10^{-9}$	$3.4(9) \times 10^{-9}$	$1.8(4) \times 10^{-9}$
50	C ₄ H ₂ ⁺ or C ₃ N ⁺	$4.1(2) \times 10^{-9}$	$9.5(4) \times 10^{-9}$	$2.5(1) \times 10^{-8}$	$1.08(3) \times 10^{-8}$	$3.7(2) \times 10^{-9}$	$1.5(1) \times 10^{-9}$	$6(1) \times 10^{-10}$
51	HC ₃ N ⁺ or C ₄ H ₃ ⁺	$1.5(2) \times 10^{-9}$	$2.0(3) \times 10^{-10}$	$2.7(3) \times 10^{-10}$	$1.4(1) \times 10^{-9}$	$1.1(4) \times 10^{-9}$	$3(1) \times 10^{-10}$	-
52	HC ₃ NH ⁺ or C ₂ N ₂ ⁺	$3.34(6) \times 10^{-8}$	$1.25(1) \times 10^{-7}$	$3.73(3) \times 10^{-7}$	$1.73(2) \times 10^{-7}$	$3.59(7) \times 10^{-8}$	$2.14(3) \times 10^{-8}$	$1.09(4) \times 10^{-8}$
53	H ₃ C ₃ N ⁺	$8(3) \times 10^{-10}$	$9(4) \times 10^{-10}$	-	-	-	-	-
54	H ₄ C ₃ N ⁺	$2.0(1) \times 10^{-9}$	$3.8(2) \times 10^{-9}$	$8.7(2) \times 10^{-10}$	$5.1(3) \times 10^{-9}$	$1.7(1) \times 10^{-9}$	$7(1) \times 10^{-10}$	-
80	C ₄ H ₄ N ₂ ⁺	$4.6(8) \times 10^{-9}$	$1.5(5) \times 10^{-9}$	$4.5(3) \times 10^{-8}$	$2.1(3) \times 10^{-8}$	$4(2) \times 10^{-9}$	$2.3(7) \times 10^{-9}$	$1.3(3) \times 10^{-9}$

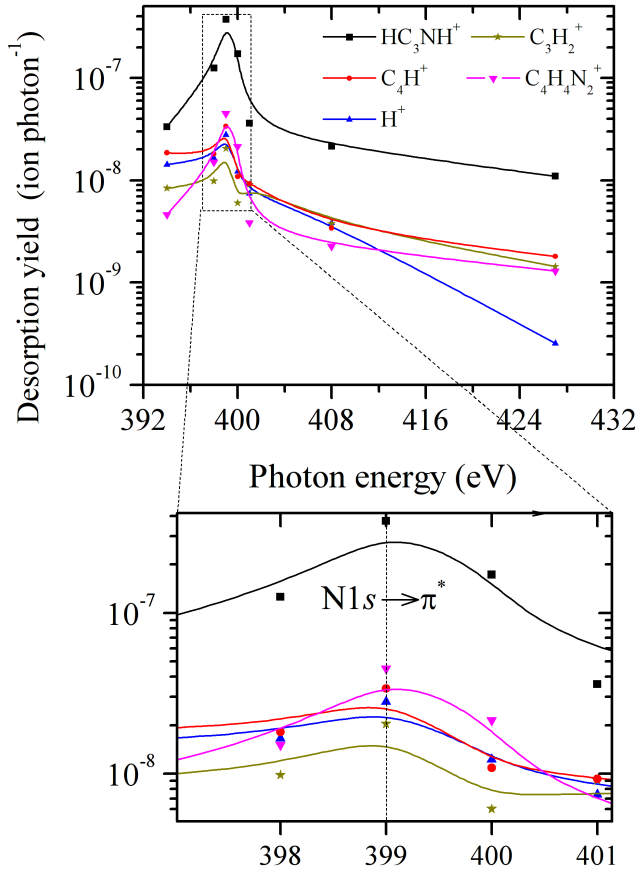

Figure 5. Desorption yield from pyrimidine ice as a function of the X-ray photon energy. The dotted line indicates the energy which gives the maximum desorption of the ionic fragments. The full lines are shown to guide the eye.

Table 4. Kinetic parameters of the photodesorption process associated with the ions listed.

m/q	Ion	Desorption process		
		Kinetic energy eV	Desorption velocity 1×10^7 cm s ⁻¹	$\Delta t/\Delta K_{pd}$ ns/eV
50	C ₄ H ₂ ⁺	12.1 ± 2.3	1.411	1.01
52	HC ₃ NH ⁺	11.4 ± 4.2	1.384	1.13
80	C ₄ H ₄ N ₂ ⁺	9.9 ± 3.1	1.116	1.44

we perform a calibration between the simulated TOF (t_s , ns) and K_{pd} (eV) for the HC₃NH⁺ ion

$$K_{pd}(\text{HC}_3\text{NH}^+) = 199 - 1.87t_s, \quad (6)$$

v_{pd} was also derived (Figure 6.a). Additionally, the $\Delta t/\Delta K_{pd}$ ratio was obtained by considering the full width of the experimental TOF. For example, as shown in Figure 6b, the fitted gaussian peak extend from 96 to 106 ns, which associates the TOF of the HC₃NH⁺ ion with its photodesorption kinetic energy.

The velocity of the photodesorbed HC₃NH⁺ ion was of the order of 10^7 cm s⁻¹, which is moderately higher than the speed of hydrogen gas at partial ionized regions, $\sim 1.5 \times 10^6$ cm s⁻¹ and, at cool regions, $\sim 1.5 \times 10^5$ cm s⁻¹ (Harwit 2006). Concerning the kinetic energy, the HC₃NH⁺ distribution is between ~ 2 and 17 eV. In order to compare the present results, it is worth mentioning Papoular 2004 calculations about hydrocarbon grain sputtering. Heavy ions like C projectiles, with velocities ~ 100 km s⁻¹ are capable of transferring up to 100 eV on amorphous hydrocarbon targets stimulating sputtering processes. On the other hand, Roser et al. 2003 determined experimentally that the thermal desorption of H₂ molecules from amorphous water ice involves energies on the order of ~ 3 meV. In Table 4 the results of C₄H₄⁺, HC₃NH⁺ and C₄H₄N₂⁺ are presented.

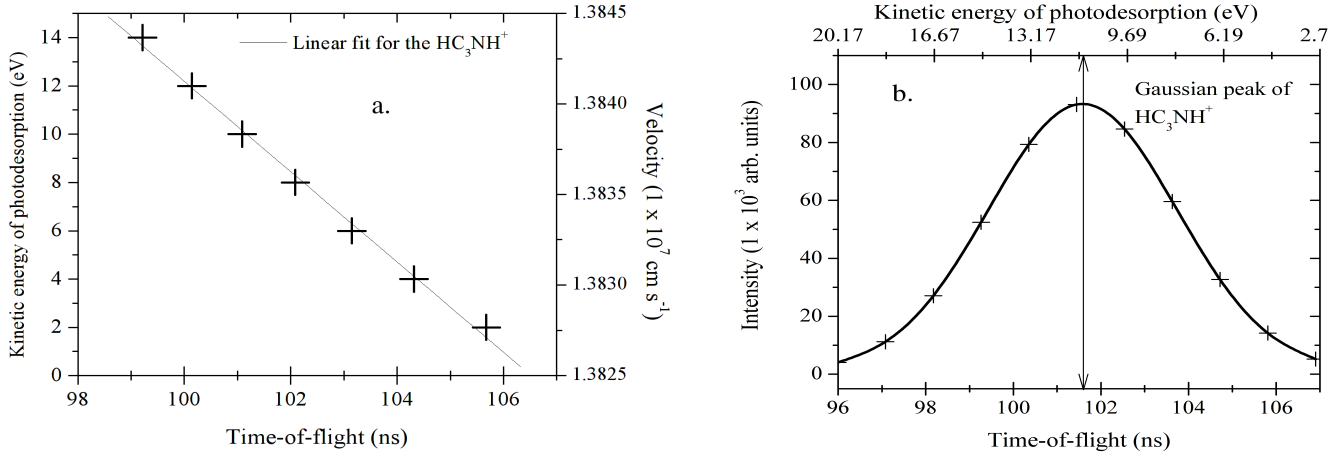


Figure 6. For the HC_3NH^+ : a. Linear fit between the kinetic energy of photodesorbed ion and the simulated TOF; the uncertainty in the fit is about $\pm 5\%$. b. Kinetic energy associated with the FWHM of the experimental peak.

4 PRODUCTION OF IONS IN PROTOPLANETARY DISKS

The formation of stars and planetary systems begins with the collapse of a molecular cloud. The young stellar objects (YSOs) can be classified based on the ratios between the envelope, star and disk masses, M_{env} , M_{star} and M_{disk} , respectively. A very interesting stage in the life of a star is when it has a circumstellar accretion disk where planets are formed. An example is TW Hydra, a young T Tauri star that has a massive face-on optically thick disk. Based on observational data, the X-ray luminosity (L_X) for TW Hydra, integrated from 0.2 to 2 keV, is $2.3 \times 10^{30} \text{ erg s}^{-1}$ (Kastner et al. 2002). Another characteristic of these newcomers stars in the pre-main sequence is the presence of intense magnetic fields that are responsible for the abrupt warming of the gas ($\sim 1 \times 10^7 \text{ K}$). In addition, magnetic reconnection events generate strong X-ray emission via the bremsstrahlung process, accompanied by the release of MeV nuclei and strong shocks that propagate into the circumstellar matter (Feigelson & Montmerle 1999; Getman et al. 2005). From observational, experimental and theoretical studies it is known that X-rays (i) are responsible for ionization and dissociation processes together with UV radiation and cosmic rays, the latter with a large contribution in the midplane of the disk; (ii) they constitute an important source of heating via Coulomb heating and H_2 ionization in the disk (up to 100 AU), because soft X-rays ($\leq 1 \text{ keV}$) are susceptible to Compton scattering (Igea & Glassgold 1999; Aresu et al. 2011); and (iii) the X-rays dominate over the UV-flux regarding photoevaporation, which extends up to 70 AU from the central star (Ercolano et al. 2008; Owen et al. 2010).

The X-ray photon flux (photons $\text{cm}^{-2} \text{ s}^{-1}$) for a given photon energy, $E = h\nu$, is given by

$$F_X(E) = \frac{L_X}{4\pi(R^2 + z^2)h\nu} \exp(-\tau), \quad (7)$$

where R and z are the radial distance and height from the midplane respectively, defining a point in the disk at a distance $r = (R^2 + z^2)^{1/2}$ from the central star. L_X is the luminosity, τ is the optical depth ($\tau = \sigma_X N_H$). The photoabsorption cross section σ_X (cm^2) for the H nucleus as a function of the X-ray photon energy $E = h\nu$ is

$$\sigma_X = \sigma_H \left(\frac{E}{1 \text{ keV}} \right)^\alpha, \quad (8)$$

where $\sigma_H = 1.155 \times 10^{-23} \text{ cm}^2$ and $\alpha = -3.4$ (Gorti & Hollenbach 2004), $N_H = n(R^2 + z^2)^{1/2}$, n being the numerical density of H. Here, we considered three n values: 1×10^6 , 1×10^7 and $1 \times 10^8 \text{ cm}^{-3}$, according to the density profiles of hydrogen in protoplanetary disks models proposed by Walsh, Millar & Nomura 2010.

Using equations (8), (7) and (3), the ion flux desorbed from the ice (f_i , ions $\text{cm}^{-2} \text{ s}^{-1}$) was obtained through the relation

$$f_i = F_X Y_i. \quad (9)$$

The ion production rate (Γ_i , ions $\text{cm}^{-3} \text{ s}^{-1}$) was then determined by

$$\Gamma_i = n_{gr} \sigma_{gr} f_i X, \quad (10)$$

where n_{gr} (cm^{-3}) is the number density; $\sigma_{gr} = \pi a^2$ (cm^2) is the cross-sectional area of the grain where a is the radius of the dust particles; X is the fraction of pyrimidine hypothetically contained in the ice mantle. In this regard, Öberg et al. 2011 determined the median ice composition toward low- and high-mass star formation. Their results indicate that the content of volatiles is minor than 10%. On the other hand, Marboeuf et al. 2008 found that the composition of ices in planetesimals formed in protoplanetary disks can vary depending on the $(\text{C}:\text{O})_{disk}/(\text{C}:\text{O})_\odot$ ratio, i.e. insofar as increases $(\text{C}:\text{O})_{disk}/(\text{C}:\text{O})_\odot$ up to ~ 2 , also rises the content of volatile in the ice, such contents does not exceed 20%. Based on those studies, we estimate pyrimidine percentages below 10%. In the Table a.1 we show the ion production rates of HC_3NH^+ stimulated by photons at 399 eV as a function of the r distance from the central star, for the numerical density values of H (a) 1×10^6 (b) 1×10^7 (c) $1 \times 10^8 \text{ cm}^{-3}$ and X (%) fraction of the grain surface covered by pyrimidine. We can clearly observe that the production of HC_3NH^+ decreases with the increasing distance. This trend is mainly due to the optical depth which increases exponentially. However, it is also observed that the ion production falls when the numerical density of hydrogen increases, which becomes greater in the regions closest to the midplane of the disk, reaching values up to 10^{12} cm^{-3} . The more pronounced exponential decay was observed considering $n = 1 \times 10^8 \text{ cm}^{-3}$, resulting in optical depths between ~ 3.9 and 47.1, with a production rate of HC_3NH^+ in the order of 10^{-10} and 10^{-31} ions $\text{cm}^{-3} \text{ s}^{-1}$, respectively. Using a density profile of $n = 1 \times 10^7 \text{ cm}^{-3}$, the optical depth falls between 0.39 and 4.71, and the production rate of HC_3NH^+ is in the order of 10^{-8} and 10^{-12} ions $\text{cm}^{-3} \text{ s}^{-1}$, respectively. Moreover, for a numerical density of $1 \times 10^6 \text{ cm}^{-3}$, we found optical depths ranging from ~ 0.04 to 0.39

Table 5. Column density of HC_3NH^+ as a function of the r distance from the central star for numerical densities of H of a. 1×10^6 and b. 1×10^7 and X (%) is the fraction of the grain surface covered by pyrimidine. The photon energy is 399 eV.

a. $n(\text{H}) = 1 \times 10^6 \text{ cm}^{-3}$					
Distance AU	Optical depth (τ)	Photon flux 1×10^7 photons $\text{cm}^{-2}\text{s}^{-1}$	HC ₃ NH ⁺ column density $1 \times 10^{11} \text{ cm}^{-2}\text{s}$		
			2 %	4 %	6 %
10	0.039	1230	111.9(9)	223(2)	335(3)
20	0.078	295.6	53.8(4)	107(9)	161(1)
30	0.117	126.3	35.5(3)	68.9(5)	103.5(8)
40	0.157	68.33	24.9(2)	49.7(4)	74.6(6)
50	0.196	42.05	19.1(1)	38.3(3)	57.4(5)
60	0.235	28.07	15.3(1)	30.7(2)	45.9(4)
70	0.274	19.83	12.6(1)	25.3(2)	37.9(3)
80	0.314	14.59	10.63(8)	21.2(2)	31.8(2)
90	0.353	11.09	9.08(7)	18.2(1)	27.2(2)
100	0.392	8.63	7.86(6)	15.7(1)	23.6(2)
110	0.432	6.86	6.87(5)	13.7(1)	20.6(2)
120	0.471	5.54	6.05(5)	12.11(9)	18.2(1)

b. $n(\text{H}) = 1 \times 10^7 \text{ cm}^{-3}$					
Distance AU	Optical depth (τ)	Photon flux 1×10^5 photons $\text{cm}^{-2}\text{s}^{-1}$	HC ₃ NH ⁺ column density $1 \times 10^9 \text{ cm}^{-2}$		
			2 %	4 %	6 %
10	0.393	8637.1	7860(63)	15721(126)	23582(189)
20	0.786	1457.8	2653(62)	5307(42)	7960(64)
30	1.178	4374.3	1194(10)	2388(19)	3583(28)
40	1.571	1661.2	604(4)	1209(9)	1814(14)
50	1.964	717.8	326(3)	653(5)	979(8)
60	2.357	336.5	183(1)	367(3)	551(4)
70	2.749	166.9	106.3(8)	212(2)	319(2)
80	3.143	86.29	62.8(5)	125.6(1)	188.5(1)
90	3.535	46.03	37.7(3)	75.4(6)	113.1(9)
100	3.928	25.17	22.9(1)	45.8(4)	68.7(5)
110	4.321	14.04	14.1(1)	28.1(2)	42.2(3)
120	4.714	7.968	8.7(6)	17.4(1)	26.1(2)

with production rates of HC_3NH^+ around of 10^{-8} and 10^{-10} ions $\text{cm}^{-3} \text{ s}^{-1}$, respectively. For practical purposes, the column density values N of HC_3NH^+ were determined integrating over 1×10^6 yr, order of magnitude corresponding to the disk lifetime, for each r distance from the central star. The results are presented in the Table 5, Figures 7a and 7b.

The HC_3NH^+ is an ion observed in interstellar conditions and was detected for first time in TMC-1 with a column density of $\sim 1 \times 10^{12} \text{ cm}^{-2}$ (Kawaguchi et al. 1994). It is important to take into account that several chemical reactions for the production and destruction of HC_3NH^+ in the gas-phase can occur, like it is shown in the Table 6. Recently, Chapillon et al. 2012 have reported the first detection of HC_3N in protoplanetary disks using IRAM 30 m array, with column densities of the order of 10^{12} cm^{-2} . It is possible that the abundance of this molecule should have some contribution due to the electron recombination reaction (equation XIV, Table 6) of the HC_3NH^+ ion produced by N-heterocyclic molecules dissociation. The formation rate of HC_3NH^+ from the chemical reaction of H_3^+ and HC_3N (equation X) can be written by

$$\frac{dn(\text{HC}_3\text{NH}^+)}{dt} = kn(\text{H}_3^+)n(\text{HC}_3\text{N}) \text{ (ions } \text{cm}^{-3}\text{s}^{-1}\text{)}, \quad (11)$$

Table 6. Chemical equations of formation and destruction of HC_3NH^+ in gaseous phase.

Equation	HC ₃ NH ⁺ formation $a + b \rightarrow \text{HC}_3\text{NH}^+ + c$	α $\text{cm}^3 \text{ s}^{-1}$
(X)	$\text{H}_3^+ + \text{HC}_3\text{N} \rightarrow \text{HC}_3\text{NH}^+ + \text{H}_2$	9.1×10^{-9}
(XI)	$\text{H}^+ + \text{CH}_2\text{CHCN} \rightarrow \text{HC}_3\text{NH}^+ + \text{H}_2$	7.5×10^{-9}
(XII)	$\text{NH}_2^+ + \text{HC}_3\text{N} \rightarrow \text{HC}_3\text{NH}^+ + \text{N}_2$	4.2×10^{-9}
(XIII)	$\text{H}_3\text{O}^+ + \text{HC}_3\text{N} \rightarrow \text{HC}_3\text{NH}^+ + \text{H}_2\text{O}$	4×10^{-9}

Equation	HC ₃ NH ⁺ destruction $\text{HC}_3\text{NH}^+ + e^- \rightarrow c + d$	α $\text{cm}^3 \text{ s}^{-1}$
(XIV)	$\text{HC}_3\text{NH}^+ + e^- \rightarrow \text{HC}_3\text{N} + \text{H}$	7.31×10^{-7}
(XV)	$\text{HC}_3\text{NH}^+ + e^- \rightarrow \text{C}_2\text{H}_2 + \text{CN}$	7.2×10^{-7}
(XVI)	$\text{HC}_3\text{NH}^+ + e^- \rightarrow \text{HNC}_3 + \text{H}$	7.50×10^{-8}
(XVII)	$\text{HC}_3\text{NH}^+ + e^- \rightarrow \text{C}_3\text{N} + \text{H}_2$	4.9×10^{-8}

where n is the abundance of the species and k is the rate coefficient given by

$$k = \alpha \left(\frac{T}{300} \right)^\beta \exp\left(-\frac{\gamma}{T}\right) \text{ (cm}^3\text{s}^{-1}\text{)}, \quad (12)$$

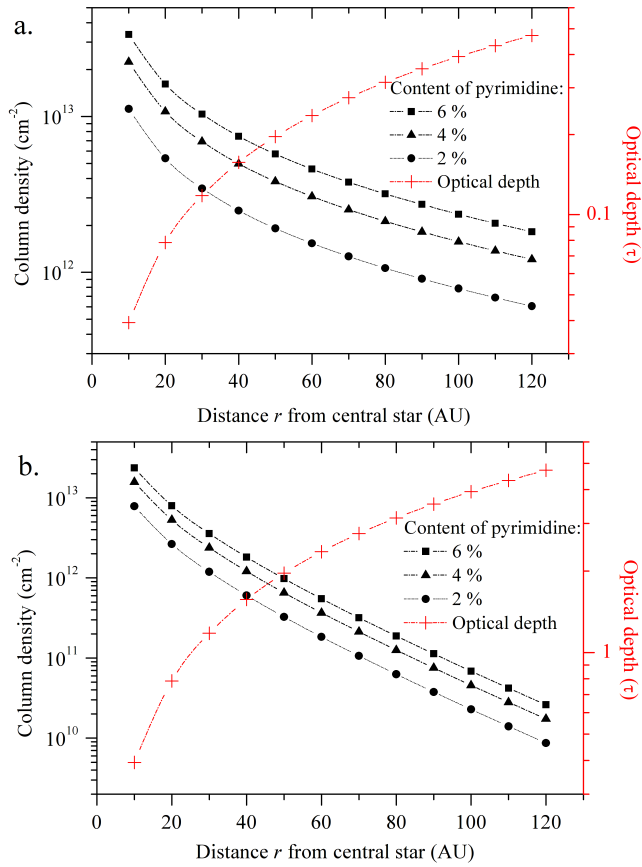


Figure 7. Column density of HC_3NH^+ as a function of the distance r from central star and of the density profiles a. $1 \times 10^6 \text{ cm}^{-3}$ and b. $1 \times 10^7 \text{ cm}^{-3}$. The squares, triangles and circles represent hypothetical content of pyrimidine of 6, 4 and 2 % in the ice, respectively. The error bars are ≤ 5 %. The dashed lines are shown to guide the eye.

where T is the temperature, α , β and γ are typical coefficients of two-body reactions (<http://www.udfa.net>, Woodall et al. 2007). Figure 8a and b presents the rate coefficients of the chemical equations listed in the Table 6. The n values were taken from Chapillon et al. 2012 and Öberg et al. 2011. They determined for the DM Tau system, in a region at a distance of 300 AU from the central star and $T \lesssim 40 \text{ K}$, the column density $N(\text{HC}_3\text{N}) \leq 3.5 \times 10^{11} \text{ cm}^{-2}$ and the fractional abundance of H_3^+ is $< 3 \times 10^{-10}$. Taking into account that the profile of $n(\text{H}) = 1 \times 10^7 \text{ cm}^{-3}$, the formation rate from the equation (X) is about $3.6 \times 10^{-16} \text{ ions cm}^{-3} \text{ s}^{-1}$. The ion production rate due to X-ray photodesorption from the pyrimidine ice, at a distance of 300 AU from central star, is about $5.1 \times 10^{-16} \text{ ions cm}^{-3} \text{ s}^{-1}$. If we consider that the formation rate of HC_3NH^+ depends on both processes described in the equations (10) and (X), the contribution of the photodesorption of N-heterocycles ices is about 59 %. This percentage is important, since for example, in the gaseous phase at $T = 30 \text{ K}$ the destruction coefficient rate (eq. XIV) is higher than formation coefficient rate (eq. X), see Figure 9. Therefore, HC_3NH^+ is more consumed than produced, so that it must have mechanisms in the condensed phase, like polymerization of molecules such as HCN and C_2H_2 or fragmentation of N-heterocycles with posterior desorption, that explain such abundances in gaseous phase.

On the other hand, gas-phase pyrimidine can be easily photo-destroyed due to UV and X-ray irradiation from the central star.

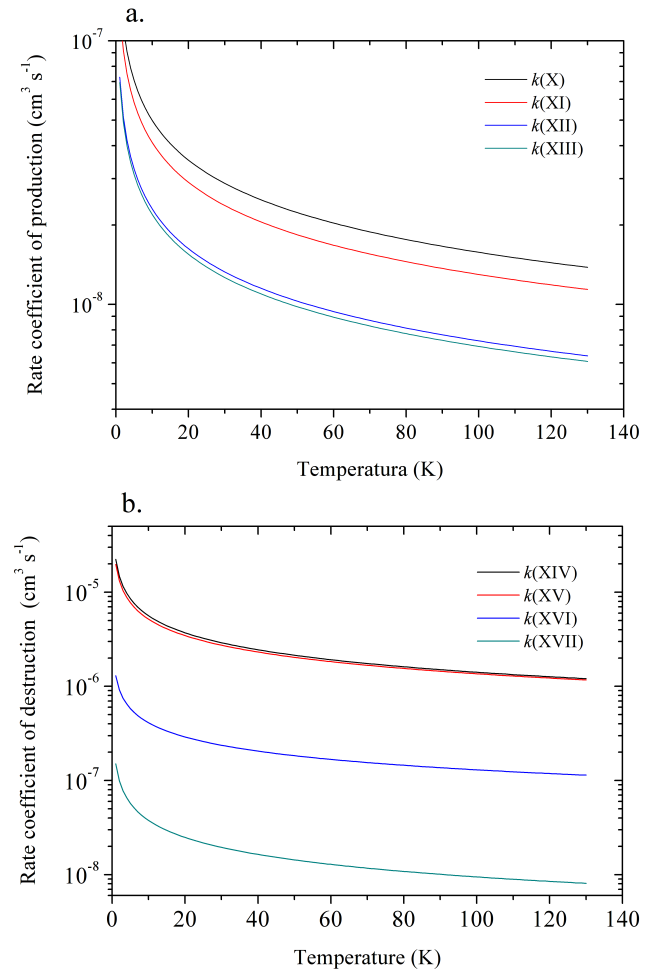


Figure 8. Rate coefficient of a. production and b. destruction of HC_3NH^+ in the gas-phase as a function of the temperature (equation 10).

The half-life of $\text{C}_4\text{H}_4\text{N}_2$ can be obtained by

$$t_{1/2} = \frac{\ln 2}{k_{ph}}, \quad (13)$$

where k_{ph} is the destruction rate and given by

$$k_{ph} = \sigma_{ph-d}(E)F_X(E), \quad (14)$$

where $\sigma_{ph-d}(E)$ is the photodissociation cross-section and $F_X(E)$ is the photon flux, both as a function of the photon energy E (equation 7). Considering that the photodissociation cross-section at N1s resonance (399 eV) of the pyrimidine is of the same order of magnitude of the photoabsorption cross-section, about $1.2 \times 10^{-17} \text{ cm}^2$ (Gas Phase Core Excitation Database, <http://unicorn.mcmaster.ca/corex/cedb-title.html>), we have obtained values of half-life as a function of the distance from the central star in the TW Hydra, according to the density profiles 1×10^6 and $1 \times 10^7 \text{ cm}^{-3}$, as shown in Figure 9. For example, $\text{C}_4\text{H}_4\text{N}_2$ molecules survive about 10 yr at a distance of 40 AU for a density of 10^7 cm^{-3} . Peeters et al. 2005, analyzing UV photons destruction, determined that the half-life of pyrimidine ice in the diffuse interstellar environment is about 8.1 yr.

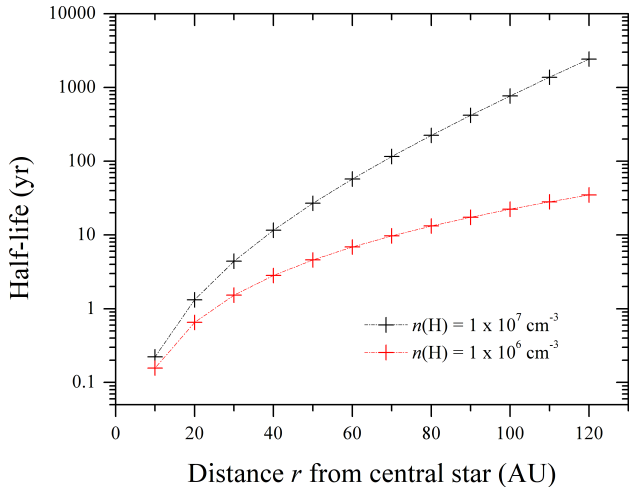


Figure 9. Half-life of the pyrimidine molecule as a function of the distance r from the central star TW Hydra. The black and red dashed lines are the half-life values for the density profiles 1×10^7 and $1 \times 10^6 \text{ cm}^{-3}$, respectively.

5 CONCLUSIONS

In this work, we present the experimental results of X-ray ionization, dissociation and desorption processes on pyrimidine ice condensed at 130 K and ionization and dissociation processes in the gas phase pyrimidine induced by H^+ at energy of 2.5 MeV. The experiments were carried out in order to estimate the production of ions from pyrimidine dissociation that can explain the high column densities of complex species in protoplanetary disks.

(i) The results show that X-ray fragmentation is more efficient to produce several different ions, since $\sim 66\%$ of the branching ratio is distributed in several ions, while using protons fragmentation is more selective, where 66% are distributed in only five ions. Considering both experiments, we highlight the formation of the following ionic series: HC_3N^+ , HC_3NH^+ , $\text{H}_2\text{C}_3\text{NH}^+$, $\text{H}_2\text{C}_3\text{NH}_2^+$ (51, 52, 53 and 54 m/q , respectively), C_4H^+ and C_4H_2^+ (49 and 50 m/q , respectively) and C^+ , C_2^+ and C_3^+ (12, 24 and 36 m/q , respectively);

(ii) Photodesorption ion yields (Y_i) of each ion (i) as a function of the photon energy were determined, where the maximum values were around 399 eV, that correspond the energy of the resonant transition $\text{N } 1s \rightarrow \pi^*$;

(iii) The simulation of the time-of-flight for the ions of equal mass, varying the initial kinetic energy from 0 to 16 eV, allowed us to determine the ratio between the FWHM of peaks and the kinetic energy distribution. For the HC_3NH^+ , C_4H_2^+ and N_2H_4^+ ions we found kinetic energies of photodesorption of 11.2 ± 3.8 , 12.1 ± 2.3 and 11.4 ± 4.2 eV, respectively. In future works, the influence of the temperature on the kinetic energies of desorbed ions should be taken into account;

(iv) Assuming three profiles of numerical density of H: 1×10^6 , 1×10^7 and $1 \times 10^8 \text{ cm}^{-3}$, production rates of HC_3NH^+ from pyrimidine ices were determined as a function of the distance from the central star. We have found that the ion production rate is affected mainly by the optical depth, obtaining values between $\sim 2.8 \times 10^{-8}$ and $7 \times 10^{-31} \text{ ions cm}^{-3} \text{ s}^{-1}$ for τ from 0.04 to 47.1;

(v) Integrating the ion production rate of HC_3NH^+ over 1 Myr, for densities of 1×10^6 and $1 \times 10^7 \text{ cm}^{-3}$, column density values, ranging from $\sim 9 \times 10^9$ to $3 \times 10^{13} \text{ cm}^{-2}$, were determined. Considering that the column density of such ion in TMC-1 is $\sim 1 \times 10^{12} \text{ cm}^{-2}$ and the destruction rate is greater than the formation rate in gaseous phase, the production of this ion (or its neutral equivalent) by X-ray photodesorption should be considered as a mechanism of chemical enrichment;

(vi) As the density affects the half-life of the pyrimidine, our results show that at a distance of 50 AU from the protostar, for density profiles of 1×10^6 and $1 \times 10^7 \text{ cm}^{-3}$, this molecule survives 4.5 and 28 yr, respectively. Those times are smaller than the half-life of protoplanetary disks, however, the photoproducts can contribute to the abundance of molecules like HC_3N already detected in systems like DM Tau, GO Tau and LkCa 15.

ACKNOWLEDGMENTS

This work was supported by CNPq, CAPES, FAPERJ and LNILS. We would like to thank the technical staff of LNILS for the valuable help during the experiments.

REFERENCES

- Andrade D. P. P., Rocco M. L. M., Boechat-Roberty H. M., 2010, MNRAS, 409, 1289
- Aresu G., Kamp I., Meijerink R., Woitke P., Thi W.-F., Spaans M., 2011, A&A, 526, 163
- Bell M. B., Feldman P. A., Travers M. J., McCarthy M. C., Gottlieb C. A., Thaddeus P., 1997, ApJ, 483, L61
- Belloche A., Garrod R. T., Müller H. S. P., Menten K. M., Comito C., Schilke P., 2009, A&A, 499, 215
- Bennett C. J., Kaiser R. I., 2007, ApJ, 661, 899
- Bera P. B., Lee T. J., Schaefer H. F., 2009, Journal of Chemical Physics, 131, 074303
- Bergin E. A., 2009, preprint (astro-ph/0908.3708)
- Bethell T. J., Bergin E. A., 2011, preprint (astro-ph/1107.3515)
- Broten N. W., MacLeod J. M., Avery L. W., Irvine W. M., Hoglund B., Friberg P., Hjalmarsen A., 1984, ApJ, 276, L25
- Chapillon E., et al., 2012, ApJ, 756, 58
- Carr J. S., Najita J. R., 2008, Sci, 319, 1504
- Cernicharo J., Heras A. M., Tielens A. G. G. M., Pardo J. R., Herpin F., Guélin M., Waters L. B. F. M., 2001, ApJ, 546, L123
- Cernicharo J., 2004, ApJ, 608, L41
- Cernicharo J., Guélin M., Agúndez M., Kawaguchi K., McCarthy M., Thaddeus P., 2007, A&A, 467, L37
- Charnley S. B., et al., 2005, Advances in Space Research, 36, 137
- Dutrey A., Guilloteau S., Guélin M., 1997, A&A, 317, L55
- Elsila J. E., Hammond M. R., Bernstein M. P., Sandford S. A., Zare R. N., 2006, Meteoritics and Planetary Science, 41, 785
- Ercolano B., Drake J. J., Raymond J. C., Clarke C. C., 2008, ApJ, 688, 398
- Farias R. H. A., 1997, Jahnel L. C., Liu Lin, Tavares P. F., eds, Proc. Particle Accelerator Conference, Optical beam diagnostics for the LNILS Synchrotron Light Source, Campinas, p. 2238
- Feigelson E. D., Montmerle T., 1999, ARA&A, 37, 363
- Fondren L. D., McLain J., Jackson D. M., Adams N. G., Babcock L. M., 2007, International Journal of Mass Spectrometry, 265, 60
- Frenklach M., Feigelson E. D., 1989, ApJ, 341, 372
- Fukuzawa K., Osamura Y., 1997, ApJ, 489, 113
- Getman K. V., et al., 2005, ApJS, 160, 353
- Glassgold A. E., Najita J., Igea, J., 1997, ApJ, 480, 344
- Gorti U., Hollenbach D., 2004, ApJ, 613, 424
- Gorti U., Dullemond C. P., Hollenbach D., 2009, ApJ, 705, 1237

- Guelin M., Green S., Thaddeus P., 1978, *ApJ*, 224, L27
- Guilhaus Michael, 1995, *Journal of Mass Spectrometry*, 30, 1519
- Harwit Martin, 2006, in *A&A library*, ed., *Astrophysical Concepts*. Springer Science+Business Media, United States, p. 395
- Hitchcock Group Home of the Canada Research Chair in Materials Research/CLS-CCRS, available at <http://unicorn.mcmaster.ca/corex/cedb-title.html>
- Hudgins D. M., Bauschlicher C. W., Jr. Allamandola L. J., 2005, *ApJ*, 632, 316
- Igea J., Glassgold A. E., 1999, *ApJ*, 518, 848
- Kastner J. H., Li J., Vrtilik S. D., Gatley I., Merrill K. M., Soker N., 2002, *ApJ*, 581, 1225
- Kawaguchi K., et al., 1991, *Publications of the Astronomical Society of Japan*, 43, 607
- Kawaguchi K., et al., 1992, *ApJ*, 396, L49
- Kawaguchi K., et al., 1994, *ApJ*, 420, L95
- Knight J. S., Freeman C. G., McEwan M. J., Smith S. C., Adams N. G., 1986, *MNRAS*, 219, 89
- Kuan Y.-J., Yan C.-H., Charnley S. B., Kisiel Z., Ehrenfreund P., Huang H.-C., 2003, *MNRAS*, 345, 650
- Lin M.-F., Dyakov Y. A., Tseng C.-M., Mebel A. M., Lin Sheng Hsien, Lee Yuan T., Nic C.-K., 2006, *Journal of Chemical Physics*, 124, 084303
- Marboeuf U., Mousis O., Ehrenreich D., Alibert Y., Cassan A., Wakelam V., Beaulieu J.-P., 2008, *ApJ*, 681, 1624
- Marques S. R., 2003, Onisto H. J., Tavares P. F., eds, *Proc. 20th IEEE Particle Accelerator Conference*, Portland, p. 3279
- Mitchell G. F., Huntress W. T. Jr., Prasad S. S., 1979, *ApJ*, 233, 102
- Nuevo M., Milam S. N., Sandford S. A., 2012, *Astrobiology*, 12, 295
- Öberg, K. I., et al., 2011, *ApJ*, 743, 152
- Öberg, K. I., et al., 2011, *ApJ*, 740, 109
- Owen J. E., Ercolano B., Clarke C. J., Alexander R. D., 2010, *MNRAS*, 401, 1415
- Papoular R., 2004, *A&A*, 414, 573
- Pardo J. R., Cernicharo J., Goicoechea J. R., 2005, *ApJ*, 628, 275
- Peeters Z., Botta O., Charnley S. B., Kisiel Z., Kuan Y.-J., Ehrenfreund P., 2005, *A&A*, 433, 583
- Petrie S., Millar T. J., Markwick A. J., 2003, *MNRAS*, 341, 609
- Pilling S., Andrade D. P. P., da Silveira E. F., Rothard H., Domaracka A., Boduch P., 2012, *MNRAS*, 423, 2209
- Pontoppidan K. M., Salyk C., Blake G. A., Meijerink R., Carr J. S., Najita J., 2010, *ApJ*, 720, 887
- Qi C., Kessler J. E., Koerner D. W., Sargent A. I., Blake G. A., 2003, *ApJ*, 597, 986
- Ricca A., Bauschlicher C. W., Bakes E. L. O., 2001, *Icarus*, 154, 516
- Roser J. E., Swords S., Vidali G., Manicò G., Pirronello V., 2003, *ApJ*, 596, L55
- Senent M. L., Hochlaf M., 2010, *ApJ*, 708, 1452
- Shanker U., Bhushan B., Bhattacharjee G., Kamaluddin, 2011, *Astrobiology*, 11, 225
- Schwell M., Jochims H.-W., Baumgärtel H., Leach S., 2008, *Chemical Physics*, 353, 145
- Solomon P. M., Jefferts K. B., Penzias A. A., Wilson R. W., 1971, *ApJ*, 168, L107
- Tachikawa H., Iyama T., Fukuzumi T., 2003, *A&A*, 397, 1
- Takagi N., Fukuzawa K., Osamura Y., Schaefer H. F., 1999, *ApJ*, 525, 791
- Thi W.-F., van Zadelhoff G.-J., van Dishoeck E. F., 2004, *A&A*, 425, 955
- Thorwirth S., Wyrowski F., Schilke P., Menten K. M., Brünken S., Müller H. S. P., Winnewisser G., 2003, *ApJ*, 586, 338
- UMIST RATE12 astrochemistry.net, available at <http://www.udfa.net>
- Vall-Llosera G., et al., 2008, *International Journal of Mass Spectrometry*, 275, 55
- Wolff W., et al., 2012, *Review of Scientific Instruments*, 83, 123107
- Woodall J., Agúndez M., Markwick-Kemper A. J., Millar T. J., 2007, *A&A*, 466, 1197
- Walsh C., Millar T. J., Nomura H., 2010, *ApJ*, 722, 1607

the author.

APPENDIX

The ion production rates, determined through the equation (10), for the profiles 1×10^6 , 1×10^7 and $1 \times 10^8 \text{ cm}^{-3}$ are listed in the table a.1.

Table a.1. Ion production rates of HC_3NH^+ as a function of the r distance from the central star for numerical densities of H of a. 1×10^6 b. 1×10^7 c. $1 \times 10^8 \text{ cm}^{-3}$ and X (%) is the fraction of the grain surface covered by pyrimidine. The photon energy is 399 eV.

a. $n(\text{H}) = 1 \times 10^6 \text{ cm}^{-3}$					
Distance AU	Optical depth (τ)	Photon flux 1×10^7 photons $\text{cm}^{-2}\text{s}^{-1}$	Ion production rate $1 \times 10^{-10} \text{ ions cm}^{-3}\text{s}^{-1}$		
			2 %	4 %	6 %
10	0.039	1230	288(2)	576(5)	865(7)
20	0.078	295.6	69.2(6)	138(1)	208(2)
30	0.117	126.3	29.6(2)	59.2(5)	88.8(7)
40	0.157	68.33	16.0(1)	32.0(2)	48.0(4)
50	0.196	42.05	9.85(8)	19.7(1)	29.6(2)
60	0.235	28.07	6.58(5)	13.2(1)	19.7(1)
70	0.274	19.83	4.65(4)	9.29(7)	13.9(1)
80	0.314	14.59	3.42(3)	6.84(5)	10.3(8)
90	0.353	11.09	2.59(2)	5.19(4)	7.79(6)
100	0.392	8.63	2.02(2)	4.05(3)	6.07(5)
110	0.432	6.86	1.61(1)	3.22(2)	4.82(4)
120	0.471	5.54	1.29(1)	2.59(2)	3.89(3)

b. $n(\text{H}) = 1 \times 10^7 \text{ cm}^{-3}$					
Distance AU	Optical depth (τ)	Photon flux 1×10^5 photons $\text{cm}^{-2}\text{s}^{-1}$	Ion production rate $1 \times 10^{-12} \text{ ions cm}^{-3}\text{s}^{-1}$		
			2 %	4 %	6 %
10	0.393	8637.1	20242(163)	40484(325)	60726(488)
20	0.786	1457.8	3416(27)	6833(55)	10249(82)
30	1.178	4374.3	1025(8)	2050(16)	3075(25)
40	1.571	1661.2	389(3)	779(6)	1168(9)
50	1.964	717.8	168(1)	336(3)	505(4)
60	2.357	336.5	78.87(6)	157(1)	237(2)
70	2.749	166.9	39.12(3)	78.2(6)	117.4(9)
80	3.143	86.29	20.22(2)	40.4(3)	60.7(5)
90	3.535	46.03	10.79(9)	21.6(2)	32.4(3)
100	3.928	25.17	5.89(5)	11.79(9)	17.7(1)
110	4.321	14.04	3.29(3)	6.58(5)	9.87(8)
120	4.714	7.968	1.86(1)	3.73(3)	5.60(4)

c. $n(\text{H}) = 1 \times 10^8 \text{ cm}^{-3}$					
Distance AU	Optical depth (τ)	Photon flux photons $\text{cm}^{-2}\text{s}^{-1}$	Ion production rate $\text{ions cm}^{-3}\text{s}^{-1}$		
			2 %	4 %	6 %
10	3.928	2.52×10^8	$5.89(5) \times 10^{-10}$	$1.18(9) \times 10^{-9}$	$1.77(1) \times 10^{-9}$
20	7.856	1.23×10^6	$2.90(2) \times 10^{-12}$	$5.80(5) \times 10^{-12}$	$8.71(7) \times 10^{-12}$
30	11.78	1.1×10^4	$2.54(2) \times 10^{-14}$	$5.07(4) \times 10^{-14}$	$7.61(6) \times 10^{-14}$
40	15.71	1.2×10^2	$2.81(2) \times 10^{-16}$	$5.62(4) \times 10^{-16}$	$8.43(7) \times 10^{-16}$
50	19.64	1.51	$3.54(3) \times 10^{-18}$	$7.07(5) \times 10^{-18}$	$1.061(8) \times 10^{-17}$
60	23.57	0.02	$4.83(4) \times 10^{-20}$	$9.67(8) \times 10^{-20}$	$1.45(1) \times 10^{-19}$
70	27.49	2.98×10^{-4}	$6.99(6) \times 10^{-22}$	$1.39(1) \times 10^{-21}$	$2.09(2) \times 10^{-21}$
80	31.43	4.49×10^{-6}	$1.053(8) \times 10^{-23}$	$2.10(2) \times 10^{-23}$	$3.17(2) \times 10^{-23}$
90	35.35	6.98×10^{-8}	$1.64(1) \times 10^{-25}$	$3.27(3) \times 10^{-25}$	$4.91(4) \times 10^{-25}$
100	39.28	1.11×10^{-9}	$2.60(2) \times 10^{-27}$	$5.22(4) \times 10^{-27}$	$7.83(6) \times 10^{-27}$
110	43.21	1.81×10^{-11}	$4.24(3) \times 10^{-29}$	$8.48(7) \times 10^{-29}$	$1.27(1) \times 10^{-28}$
120	47.13	2.99×10^{-13}	$7.01(5) \times 10^{-31}$	$1.40(1) \times 10^{-30}$	$2.10(2) \times 10^{-30}$